J. Fluid Mech. (2011), *vol.* 683, *pp.* 149–171.
doi:10.1017/jfm.2011.257

Inertial effects on the dynamics, streamline topology and interfacial stresses due to a drop in shear

Rajesh Kumar Singh and Kausik Sarkar†

Department of Mechanical Engineering, University of Delaware, Newark, DE-19716, USA
Biomechanics and Movement Science Program, University of Delaware, Newark, DE-19716, USA

(Received 1 November 2010; revised 27 April 2011; accepted 3 June 2011;
first published online 19 August 2011)

Deformation of a viscous drop in shear at finite inertia and the streamlines around it are numerically investigated. Inertia destroys the closed streamlines found in Stokes flow. It creates reversed streamlines and streamlines spiralling around the vorticity axis. Spiralling streamlines spiral either towards the central shear plane or away from it depending on the viscosity ratio and the inertia. The zones of open or reversed streamlines as well as streamlines spiralling towards or away from the central shear plane are delineated for varying viscosity ratio and Reynolds number. In contrast to the infinite extent of the closed Stokes streamlines around a rigid sphere in shear, the region of the spiralling streamlines in the vorticity direction both for a rigid sphere and a drop shrinks with inertia. Inertia increases deformation, and introduces oscillations in drop shape. An approximate analysis explains the scaling of oscillation frequency and damping with Reynolds and capillary numbers. The steady-state drop inclination angle with the flow axis increases with increasing Reynolds number for small Reynolds number. But it decreases at higher Reynolds number, especially for larger capillary numbers. For smaller capillary numbers, drop inclination reaches higher than 45° (the direction of maximum extension), critically affecting the interfacial stresses due to the drop. It changes the sign of first and second normal interfacial stress differences (and thereby these components of the effective stresses of an emulsion of such drops). Increasing viscosity ratio orients the drop towards the flow axis, which increases the critical Reynolds number above which the drop inclination reaches more than 45°.

Key words: drops, emulsions, rheology

1. Introduction

Rheology of an emulsion or a suspension is governed by the microstructure (particles' shape, deformation and spatial positioning) and the underlying interactions (between multiple particles). The problem has almost exclusively been studied in the inertia-less Stokes flow limit; see the reviews by Leal (1980), Rallison (1980) and Stone (1994). However, even a small amount of inertia (particle Reynolds number $\sim O(1)$) can profoundly affect deformation (Sarkar & Schowalter 2001*a*,*b*; Li & Sarkar 2005*b*,*d*, 2006), flow field (Mikulencak & Morris 2004; Subramanian & Brady 2006;

† Email address for correspondence: sarkar@udel.edu

Subramanian & Koch 2006*a*) and rheology (Li & Sarkar 2005*a*,*c*; Kulkarni & Morris 2008*b*; Raja, Subramanian & Koch 2010), giving rise to a fundamentally different streamline pattern, particle trajectories (Kulkarni & Morris 2008*a*; Olapade, Singh & Sarkar 2009; Singh & Sarkar 2009) and unusual rheological effects such as change in sign of effective normal stress differences of the emulsion (Li & Sarkar 2005*a*,*c*; Raja *et al.* 2010). Streamline patterns and the stresses due to a rigid cylinder or a sphere in shear at finite inertia have been investigated in detail (Lin, Perry & Schowalter 1970; Kossack & Acrivos 1974; Poe & Acrivos 1975; Mikulencak & Morris 2004; Subramanian & Koch 2006*a*,*b*). Here we study the corresponding problem of a drop, namely, drop deformation, streamlines around it and the stresses created by it in a shear flow at finite inertia.

In a Stokes flow, shear generates closed streamlines around and near a sphere and open streamlines away from it. The closed streamlines assume critical importance in transport phenomena: for example, because of them, even at infinite Péclet number, the heat transfer from a sphere or cylinder remains small (Acrivos 1971). Perturbation analysis of inertial effects for cylinders has indicated that circular closed streamlines, and thereby small heat transfer, persist (Robertson & Acrivos 1970*a*,*b*; Kossack & Acrivos 1974) at small inertia. For a sphere, although a perturbative solution became available around the same time (Lin *et al.* 1970), it was realized only recently that inertia destroys the closed streamlines, transforming them into spiralling ones, leading to enhanced heat transfer at finite Péclet numbers (Subramanian & Koch 2006*a*,*b*). Inertia also introduces a zone of reversed streamlines fore and aft of the sphere. Altered streamlines lead to reversed and spiralling trajectories for a particle pair (Kulkarni & Morris 2008*a*). For the same reason, our recent investigation found two types of trajectories: passing type I and reversed type II for a drop-pair in shear (Olapade *et al.* 2009; Singh & Sarkar 2009). Here we investigate how drop deformation affects the streamline pattern. In a suspension, stresses generated by the suspended particles (stresslet field in the far field) contribute towards the effective shear and normal stresses for the overall system. In a Stokes suspension of rigid spheres, in the dilute limit, one obtains the classical result due to Einstein, namely an increased shear viscosity $\mu_{eff}/\mu_m = (1 + 2.5\phi)$ (μ_m is the matrix viscosity and ϕ is the volume fraction) and no normal stresses. In a sheared emulsion, on the other hand, one obtains positive first normal stress difference and negative second normal stress difference due to deformed drops inclined towards the flow direction (Choi & Schowalter 1975). However, finite inertia leads to a sign change, i.e. negative first normal stress and positive second normal stress differences (Li & Sarkar 2005*c*; Raja *et al.* 2010). This can be traced to the stresses produced by a single drop. Here we investigate in detail the interfacial stresses (interface tensor) due to a drop at finite inertia and how they are affected by the drop shape.

We use a front-tracking finite difference method (Unverdi & Tryggvason 1988; Tryggvason *et al.* 2001) that we have applied to a number of different problems involving drop deformation at finite inertia (Sarkar & Schowalter 2001*a*; Li & Sarkar 2005*b*, 2006; Olapade *et al.* 2009) as well as viscoelasticity (Aggarwal & Sarkar 2007, 2008*a*,*b*; Mukherjee & Sarkar 2009, 2010, 2011). The problem setup is described in § 2. In § 3, we first study the effects of Reynolds number on streamlines around a rigid sphere and compare them with previous results. Then we study the same for a deforming drop, varying various parameters such as Reynolds number, capillary number and the viscosity ratio. We investigate drop deformation, inclination, streamlines around it and the interfacial stresses (interface tensor) from a single drop that governs the far field and appears in rheological expressions of an emulsion. In § 4,

we summarize the present work. In Appendices A and B, we provide mathematical formulations describing the role of interface tensor in emulsion rheology and far-field effects due to a drop.

2. Problem setup

We put a spherical drop at the centre of a cubical computational box of size $15a \times 15a \times 15a$ (a is the undeformed drop radius) with a uniform grid resolution of $144 \times 144 \times 144$ and initially 9248 grid points for the discretization of the drop surface (note that as the drop deforms, its surface is adaptively regridded). Periodic boundary conditions are imposed along the x (velocity) and z (vorticity) directions. The upper y-wall of the domain moves to the right with velocity U and the lower wall moves to the left with $-U$, thereby generating a simple shear of magnitude $\dot{\gamma}$. The initial condition of the problem is assumed to be a simple shear where a spherical drop of radius a is suddenly introduced. Mathematical formulation and the front-tracking implementation are discussed in detail in earlier references (Sarkar & Schowalter 2001*a*; Li & Sarkar 2005*b*). The effects of the domain size and the grid resolution have also been studied in our previous publications (Olapade *et al.* 2009; Singh & Sarkar 2009): confinement increases drop alignment with the flow (Sibillo *et al.* 2006). Here, we carefully perform simulations till a drop reaches the steady-state shape ($t' = t\dot{\gamma} \sim 10$). We use the radius of the undeformed drop a as the length scale and the advection time $\dot{\gamma}^{-1}$ as the time scale to define various dimensionless parameters in the problem: Reynolds number $Re = \rho_m \dot{\gamma} a^2/\mu_m$, capillary number $Ca = \mu_m \dot{\gamma} a/\Gamma$ and viscosity ratio $\lambda = \mu_d/\mu_m$. The symbol ρ is the density, μ is the viscosity, and Γ is the interfacial tension. Subscripts m and d relate to the matrix and the dispersed phases. Also note that, previously, we compared our simulation of drop deformation (Li & Sarkar 2005*c*) with experimental measurements of Guido & Villone (1998) and the analytical theory of Almusallam, Larson & Solomon (2004). We also compared very well with experimental observations by Guido & Simeone (1998) of binary collision between polydimethylsiloxane (PDMS) drops in polyisobutylene (PIB) matrix (Olapade *et al.* 2009).

3. Results and discussions

3.1. *Flow past a rigid sphere*

Tanaka & Araki (2000) have recently shown that in a numerical simulation with a single fluid formulation such as the one adopted here, spherical drops with $\lambda \geqslant 50$ behave like rigid spheres. In this section, we choose $\lambda = 150$ (the higher λ was required to get the right kind of spiralling streamlines below) to simulate effects of inertia on the flow around a freely rotating rigid sphere in shear. Because the code is explicit, and therefore cannot simulate zero Reynolds number, we use $Re = 0.02$ as a case representative of small Reynolds numbers. In Stokes flow, one sees two types of streamlines, open and closed. At this Reynolds number, we see open streamlines away from the drop. However, near the drop, the streamlines are actually spiralling around the drop instead of being closed (figure 1*a*). As mentioned above, inertia destroys the closed Stokes streamlines around the sphere; a fluid element here (which was earlier in the closed streamline zone) spirals around the vorticity axis before departing to infinity.

With increasing inertia, there appear clear zones of reversed streamlines fore and aft of the sphere (figure 1*b*,*c*). Fluid particles away from the sphere (not participating in spiralling) can either pass in an open or a reversed streamline. The zone of reversed

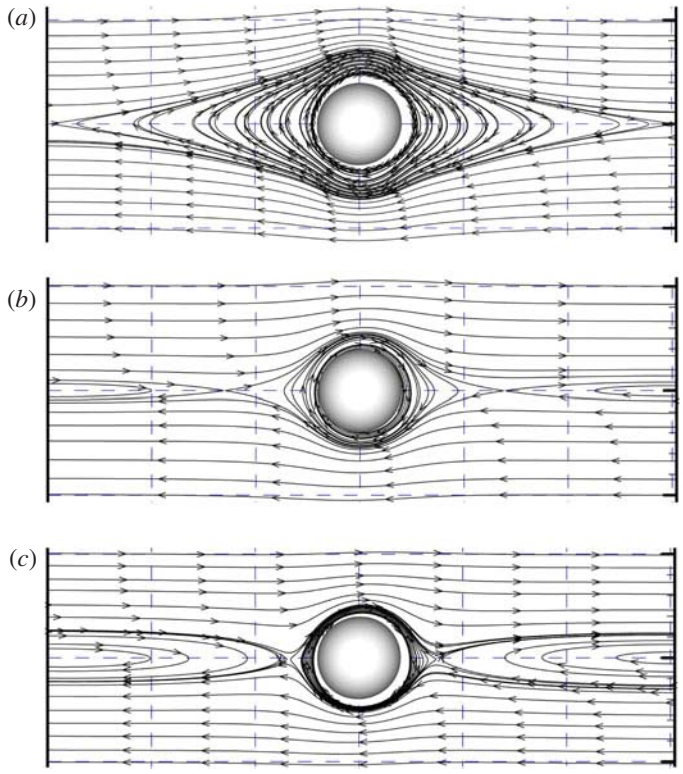

FIGURE 1. (Colour online available at journals.cambridge.org/flm) Streamlines at the central shear plane for a rigid sphere at different Re: (a) $Re = 0.02$, (b) $Re = 0.5$, (c) $Re = 2$.

streamlines meets the zone of spiralling streamlines at a stagnation point. Poe & Acrivos (1975) and Mikulencak & Morris (2004) showed that the stagnation point moves closer to the sphere with increasing inertia. In figure 2, simulated distance of the stagnation point obtained with the present code matches well with the experimental observations (Poe & Acrivos 1975) and finite element simulation (Mikulencak & Morris 2004) of these references.

In figure 3(a), we show three different kinds of in-plane streamlines around a rigid sphere at $Re = 1.0$. Figure 3(b) shows projections of an off-plane spiralling streamline passing through $(-0.05a,\ 0,\ 3.3a)$ in the x–z and x–y planes. Off-plane spiralling streamlines come closer to the central shear plane, and then depart to infinity in the flow direction (Subramanian & Koch 2006b). The streamline can be understood by considering a rotating fluid element near the particle surface which feels a centrifugal force due to rotation. The force being stronger (larger radius of curvature) near the central shear plane, fluid elements there spiral radially outward, and continuity makes fluid come towards the central plane along the vorticity direction.

Note that the direction and position of departure of a streamline depends on the location of the initial point of the streamline. For instance, far away in the vorticity direction, streamlines do not participate in a spiralling trajectory and become either reversed or open trajectory. This is in contrast to the Stokes streamlines around a rigid sphere in shear, where the region of the closed streamlines extends to infinity in the vorticity direction. Here z_s is the distance along the vorticity axis from the

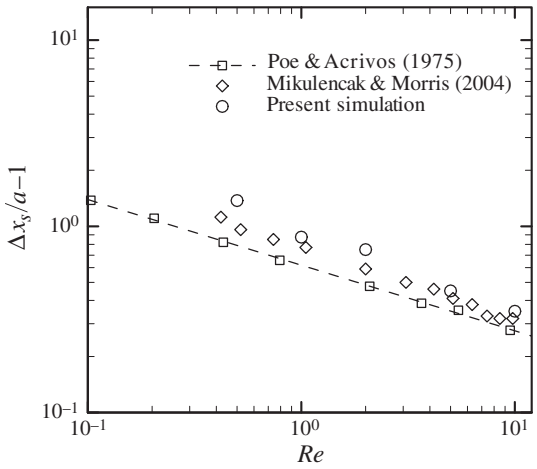

FIGURE 2. Distance of the stagnation point separating closed streamlines from reversed streamlines around a rigid sphere in shear.

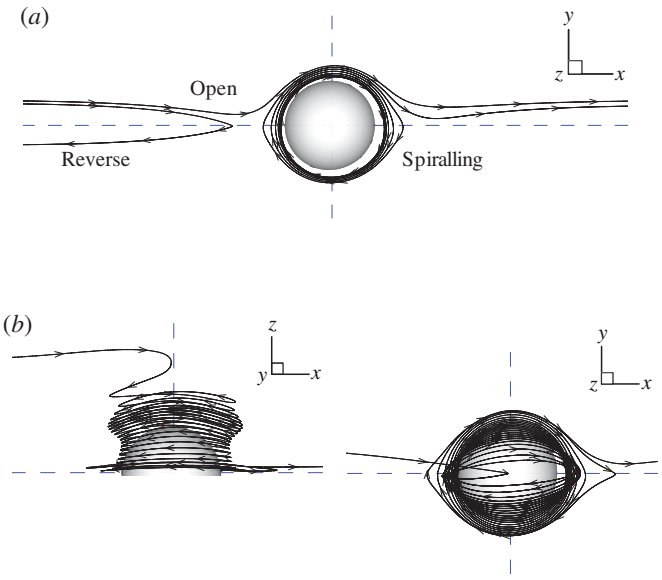

FIGURE 3. (Colour online) (*a*) In-plane open streamline (through $-2.20a$, $0.25a$, 0), reversed streamline (through $-2.20a$, 0, 0) and spiralling streamline (through $-1.09a$, 0, 0). (*b*) Off-plane spiralling streamline (through $-0.05a$, 0, $2.30a$) around a rigid sphere projected onto the x–z and x–y planes at $Re = 1.0$ in a shear flow.

particle centre, that separates spiralling trajectories from non-spiralling ones. It shrinks very close to the particle surface as the Reynolds number is increased (figure 4). It should be noted that inadequate (small) domain size in the vorticity direction leads to smaller z_s; we investigated this effect by progressively increasing the domain size and the z_s plotted here is independent of domain size. The finite extent of the region of spiralling can be explained by noting that increased inertia moves fluid particles quickly past the sphere surface in a less curved open configuration. For a rigid

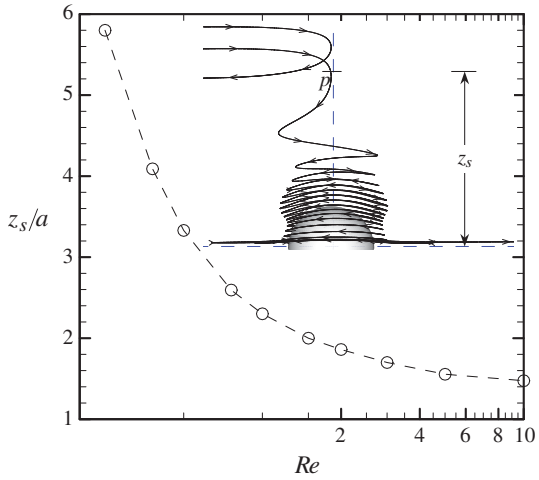

FIGURE 4. (Colour online) Distance z_s marking the extent of the domain of spiralling streamlines around a rigid sphere in shear with Reynolds numbers. The inset shows an off-plane spiralling streamline and a reversed streamline projected onto the x–z plane at $Re = 0.50$.

sphere, we find spiralling streamline moving towards the central plane for the range of Reynolds number investigated, $Re < 10$. It should be contrasted with the case of a drop to be discussed later, where we find a region of streamlines spiralling away from the central plane.

3.2. *Effects of inertia on drop deformation and inclination*

The existing literature on the inertial effects on drop dynamics is focused on inertial breakup (Renardy & Cristini 2001*a*,*b*; Renardy 2008), showing that inertia facilitates breakup. In contrast, here we consider cases where the drop attains a steady shape without breakup. In figure 5(*a*), we present the evolution of Taylor deformation $D = (L - B)/(L + B)$ with t' for $Ca = 0.01$ at different Reynolds numbers. (The Taylor criterion is based on the fact that the drop assumes an approximately ellipsoidal shape; L and B are its major and minor axes.) As expected, higher inertia results in a larger drop deformation. Initially, there are transient overshoots and oscillations in deformation due to inertia, and later the drop reaches a steady shape. Note that such oscillations have been observed before in a breakup study (Renardy & Cristini 2001*a*). However, oscillations disappear at a higher capillary number, $Ca = 0.15$ (figure 5*a* inset). The oscillatory transient response of the drop deformation can be explained by a one-dimensional mass–spring system. We represent deformation by the displacement variable X (dimensionless) of a mass–spring system, following a similar treatment executed before (Sarkar & Schowalter 2000, 2001*a*; Renardy & Cristini 2001*a*; Li & Sarkar 2005*b*, 2006). We use a modified version of the same equation,

$$\rho a^4 \ddot{X} + \mu a^2 \dot{X} + \Gamma a X = \mu a^2 \dot{\gamma} + \rho a^4 \dot{\gamma}^2, \tag{3.1}$$

where the terms on the left represent force due to acceleration of the drop, viscous resistance and interfacial tension, respectively. The first term on the right represents the forcing due to the viscous stretching. We add a second force representative of the convective term $\sim \rho(\boldsymbol{u} \cdot \nabla \boldsymbol{u})a^2$. Note that the terms are only representative and do not contain quantitative information (e.g. the actual numerical factor), and can therefore

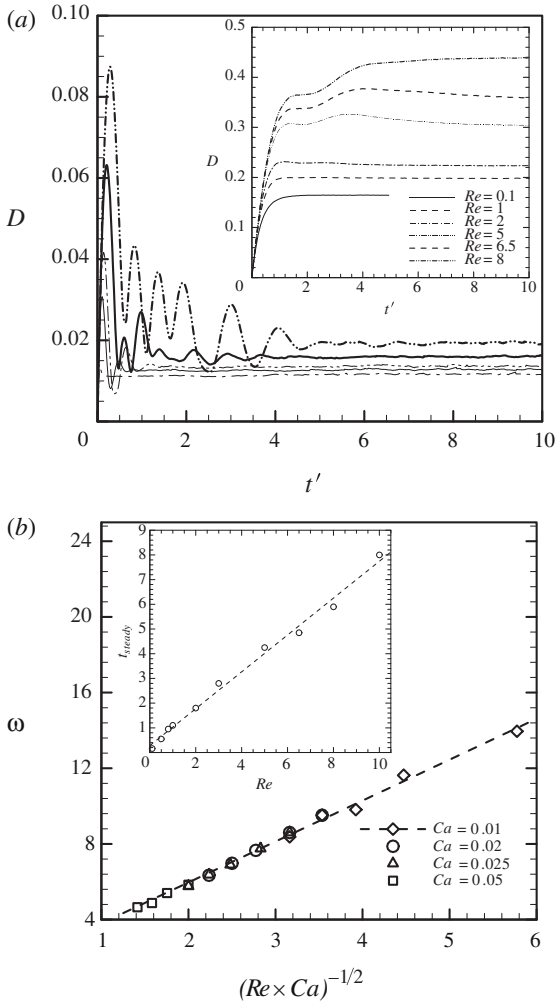

FIGURE 5. (*a*) Deformation of drop versus time at different *Re* and $Ca = 0.01$. The inset shows the same plot at $Ca = 0.15$. (*b*) Frequency of oscillation in deformation with $Re \times Ca$. The inset shows the time to reach steady drop deformation with *Re*.

only be used for scaling analysis. Rearranging and using $\dot{\gamma}^{-1}$ as a time scale gives

$$\ddot{X} + \frac{1}{Re}\dot{X} + \frac{1}{Re\,Ca}X = \frac{1}{Re} + 1. \tag{3.2}$$

This equation predicts a natural frequency $\sim(Re\,Ca)^{-1/2} = We^{-1/2}$; *We* is the Weber number. The simulated transient oscillation in deformation is seen to satisfy this relation (figure 5*b*). The frequency of oscillation is approximately evaluated by estimating the number of oscillations in the initial time interval before the oscillation dies down. The decay rate of the oscillation predicted by the model is $\sim Re^{-1}$. Accordingly, in the inset of figure 5(*b*), the time t_{steady}, when the oscillation has decayed and the deformation becomes constant, shows a linear rise with *Re*. A similar analysis using a homogeneous damped-mass–spring model was used to explain the scaling of the period of oscillation and the decay rate in a previous numerical

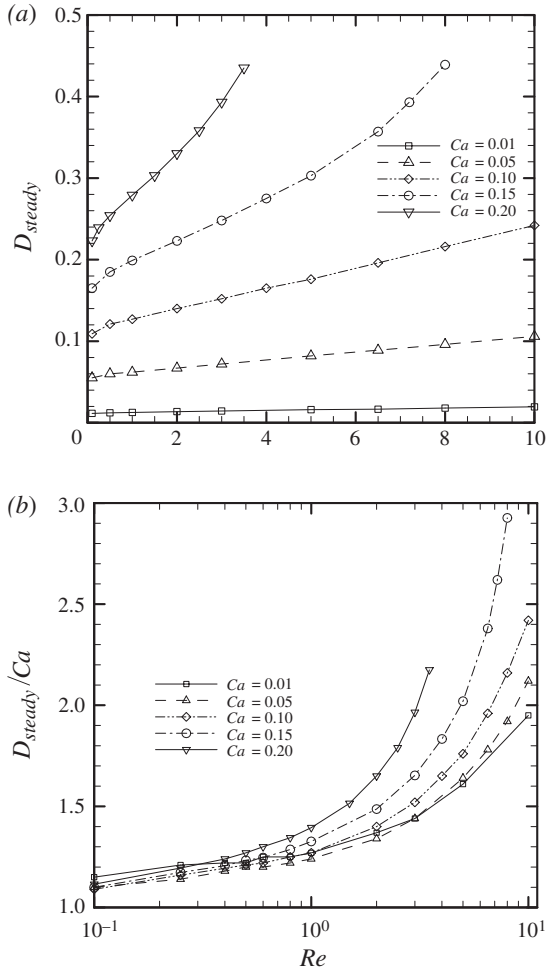

FIGURE 6. (*a*) Steady deformation (D_{steady}) versus *Re* for different *Ca*, (*b*) D_{steady}/Ca with *Re*.

simulation (Renardy & Cristini 2001*a*). However, we note that the exact form (3.1) of the ODE, specifically the inertial and viscous forcing on the right-hand side, is different, and this proves critical for predicting the steady-state response described below. The lack of oscillation for the larger value of $Ca = 0.15$ can also be explained by the ODE model, in that larger *Ca* leads to an overdamped system.

In figure 6(*a*), we plot the steady-state drop deformation as a function of Reynolds number for several *Ca* values. In a Stokes flow, the steady deformation is determined by the balance of the viscous stretching and the interfacial tension embodied by the capillary number. Perturbation analysis predicts the linear relation due to Taylor: $D_{st} = (19\lambda + 16)/(16\lambda + 16)Ca$ (Taylor 1934). Drop inertia increases the deformation. The ODE in (3.2) predicts the steady-state response as $X \sim Ca(1 + Re)$. We plot D/Ca as a function of *Re*, which shows a linear variation (figure 6*b*). Note that the model also captures the Stokes behaviour of small deformation $D \sim Ca$, in that curves for all *Ca* values overlap for small *Re*. For the highest two values of capillary number considered, $Ca = 0.15, 0.20$, one finds that there is no steady state beyond $Re = 8$ and

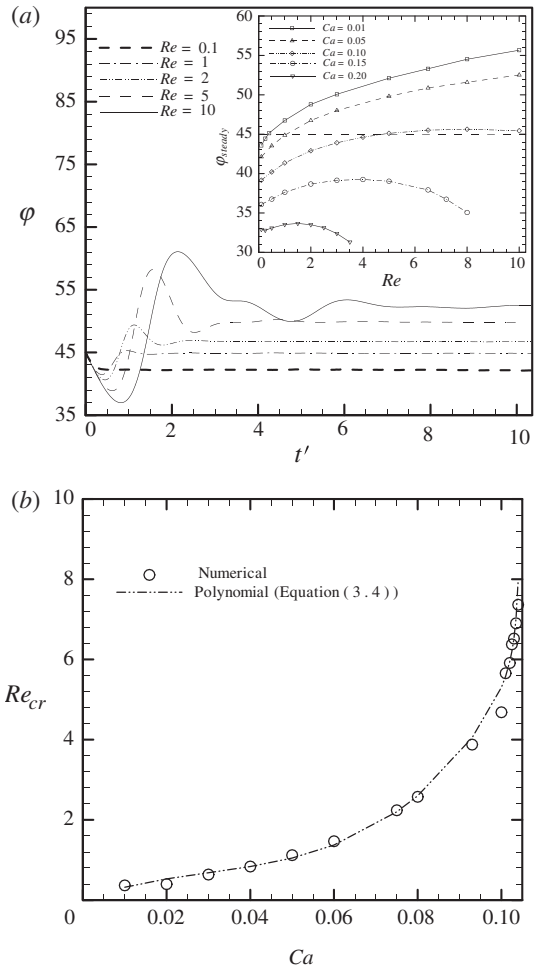

FIGURE 7. (*a*) Drop orientation for different Re at $Ca = 0.05$. The inset shows steady-state orientation φ_{steady} with Re for different Ca. (*b*) The critical Reynolds number Re_{cr} above which $\varphi > \pi/4$, as a function of Ca.

$Re = 3.5$ respectively (figure 6*a*), in good agreement with a previous study of inertial drop breakup (Renardy & Cristini 2001*b*).

In figure 7(*a*), we plot the time evolution of drop inclination (measured positive anticlockwise) for $Ca = 0.05$ for different Reynolds numbers. The shear has its extension axis oriented at $\pi/4$ to the flow axis. Therefore the drop's inclination starts at that angle, and in a Stokes flow becomes smaller than $\pi/4$ as the drop elongates and correspondingly gets subjected to a larger turning moment. To second order in Ca, the inclination is (Chaffey & Brenner 1967)

$$\varphi = \frac{\pi}{4} - \frac{(2\lambda + 3)(19\lambda + 16)}{80(\lambda + 1)} Ca. \tag{3.3}$$

We find similar behaviour for the lowest $Re = 0.1$. Inertia introduces oscillation in inclination evolution as it does for deformation. The oscillation dies down, and the inclination reaches a steady state. The steady inclination increases with inertia as

has also been found previously (Renardy & Cristini 2001*a*; Li & Sarkar 2005*c*). At higher Ca, inclination, like deformation, is overdamped and does not oscillate (not shown here) for the reason mentioned earlier. In the inset of figure 7(*a*), steady-state inclination is plotted as a function of Reynolds number for several capillary numbers. It increases with Reynolds number, and most importantly reaches a value larger than $\pi/4$. This has crucial effects on the emulsion rheology, in that it changes the sign of normal stress differences (see § 3.3 below). As we have seen before, the deformation increases with Reynolds number; the increasing torque for the increased drop length eventually hinders inclination increase at higher Re. We expect increased capillary number to have a similar effect due to increased deformation. In fact, for $Ca = 0.15, 0.20$, one sees that the inclination eventually decreases, and never reaches above $\pi/4$. In figure 7(*b*), we plot the critical Reynolds number Re_{crit} – where the angle increases above $\pi/4$ – as a function of capillary number. We see a scaling $Re_{crit} \propto Ca$ for small Ca values. This is consistent with the perturbation results in terms of the Ohnesorge number $Oh = \sqrt{Ca/Re}$(see § 3.3). One can understand the Oh-dependence by noting that, at small capillary number and inertia, increasing Ca decreases inclination and increasing Re increases inclination; the competition is embodied by their ratio. However, we have noted in the inset of figure 7(*a*) that, for larger capillary numbers (0.15 and 0.20), the angle never reaches $\pi/4$. Indeed, by carefully investigating many simulations, we have determined that at around $Ca \approx 0.105$, Re_{crit} becomes infinite. The simulated values of Re_{crit} suggests the following empirical relation, plotted in the same figure (figure 7*b*):

$$Re_{crit} = \frac{4.143Ca(1 - 30.71Ca + 437.4Ca^2 - 2239Ca^3)}{0.105 - Ca}. \tag{3.4}$$

3.3. *Interface tensor at finite inertia*

Batchelor (1970) provided a formulation that relates the bulk stresses in an emulsion to the individual stresses that are generated by the suspended drops. In Appendices A and B, we provide brief descriptions of the theory for an emulsion and the far-field expression due to a drop, respectively. The first one shows that the interface tensor $\boldsymbol{q}$, a purely geometric quantity, contributes to the interfacial part $\boldsymbol{\sigma}^{int}$ of the effective stress $\boldsymbol{\sigma}^{avg}$ of an emulsion (see (A 5)). In Appendix B, we see that the far field (B 10) for a force-free drop is also governed by the interface tensor. This tensor $\boldsymbol{q}$ is defined by

$$\boldsymbol{q} = \int_{A_d} (\boldsymbol{I} - \boldsymbol{nn})\, \mathrm{d}A, \tag{3.5}$$

where $\boldsymbol{I}$ is the identity tensor, $\boldsymbol{n}$ is the outward normal, and the integral is over the drop interface.

The first interfacial normal stress difference ($N_1^{int} = \sigma_{11}^{int} - \sigma_{22}^{int}$) is proportional to the difference $q_{11} - q_{22}$ (see (A 5)). Typically in a Stokes flow, $q_{11} - q_{22} > 0$, giving rise to a positive first normal stress difference, and correspondingly a negative second normal stress difference ($N_2^{int} = \sigma_{22}^{int} - \sigma_{33}^{int} \propto q_{22} - q_{33} < 0$). However, the presence of drop inertia alters the sign of these normal stress differences: N_1^{int} becomes negative and N_2^{int} positive for a range of Reynolds and capillary numbers (Li & Sarkar 2005*c*). In fact, interfacial contribution at this range is much larger than the inertial perturbation stress ($\boldsymbol{\sigma}^{vis} = 0$ for a viscosity matched system, and $\boldsymbol{\sigma}^{ptb}$ is small), effecting an identical sign change on the overall first and second normal stress differences (Li & Sarkar

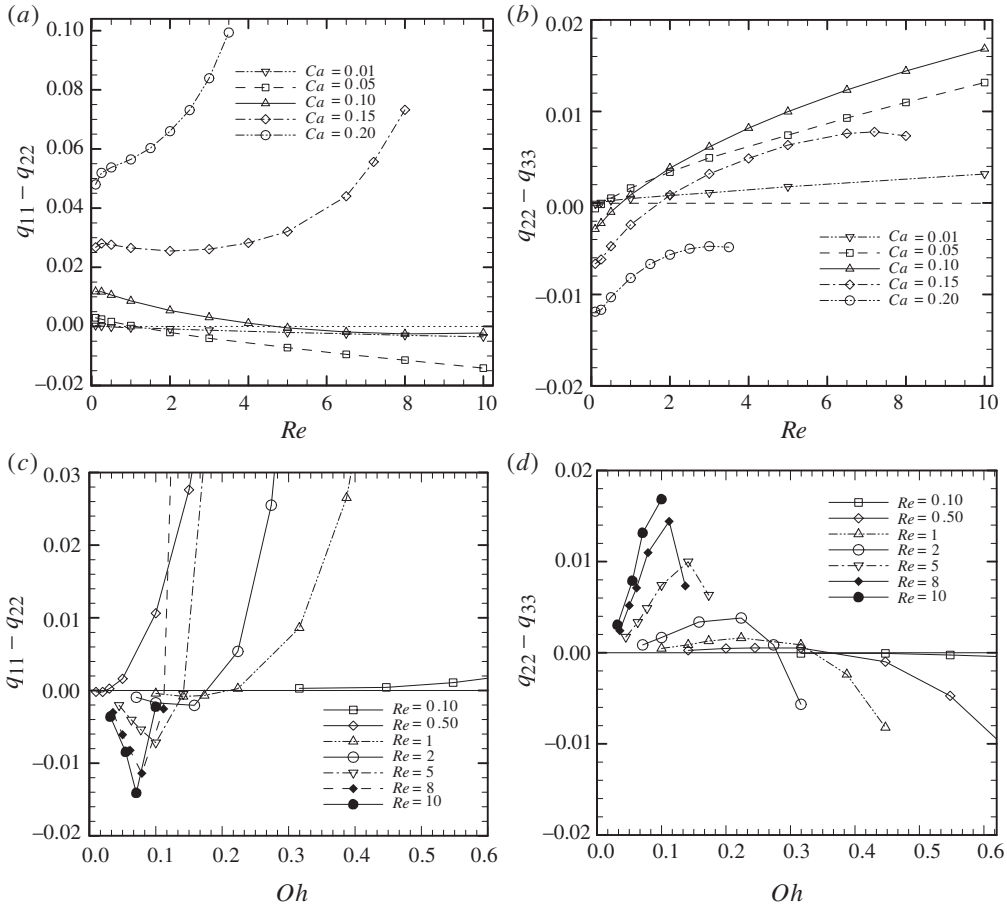

FIGURE 8. Steady-state interface tensor differences $q_{11} - q_{22}$ (*a*) and $q_{22} - q_{33}$ (*b*) with *Re* for different *Ca*. Steady-state interface tensor difference $q_{11} - q_{22}$ (*c*) and $q_{22} - q_{33}$ (*d*) with *Oh* for different *Re*.

2005*c*; Raja *et al.* 2010). The change in sign of the first normal stress difference is due to an inclination $\varphi > \pi/4$ with the flow direction (figure 7). At $\varphi = \pi/4$, $q_{11} = q_{22}$, and correspondingly for $\varphi > \pi/4$, $q_{11} - q_{22} < 0$.

In figures 8(*a*) and 8(*b*), we plot the first and second interface tensor differences $q_{11} - q_{22}$ and $q_{22} - q_{33}$ as functions of *Re* for several *Ca* values. At the lowest value $Re = 0.1$, $q_{11} - q_{22}$ is positive for all values of *Ca* considered. It is also positive for all *Re* for higher values of capillary numbers ($Ca \geqslant 0.15$). However, for lower capillary numbers, it becomes negative at larger *Re*. One can also note that it occurs when $\varphi > \pi/4$ in figure 7(*a*). The variation of the interfacial tensor difference with *Re* mimics what we see for the inclination. It decreases due to increasing inclination at least initially. For higher *Ca* values, it eventually increases as the inclination decreases with more deformed drops. For $Ca \leqslant 0.1$, the critical *Re* for achieving negative $q_{11} - q_{22}$ increases with *Ca*. When *Re* is increased, increased φ results in a larger q_{22}. This in turn makes $q_{22} - q_{33}$ increase with *Re*, as can be seen in figure 8(*b*). For smaller capillary numbers $Ca \leqslant 0.15$, it leads to positive $q_{22} - q_{33}$, in contrast to results in Stokes flows. Like $q_{11} - q_{22}$, sign change in $q_{22} - q_{33}$ occurs

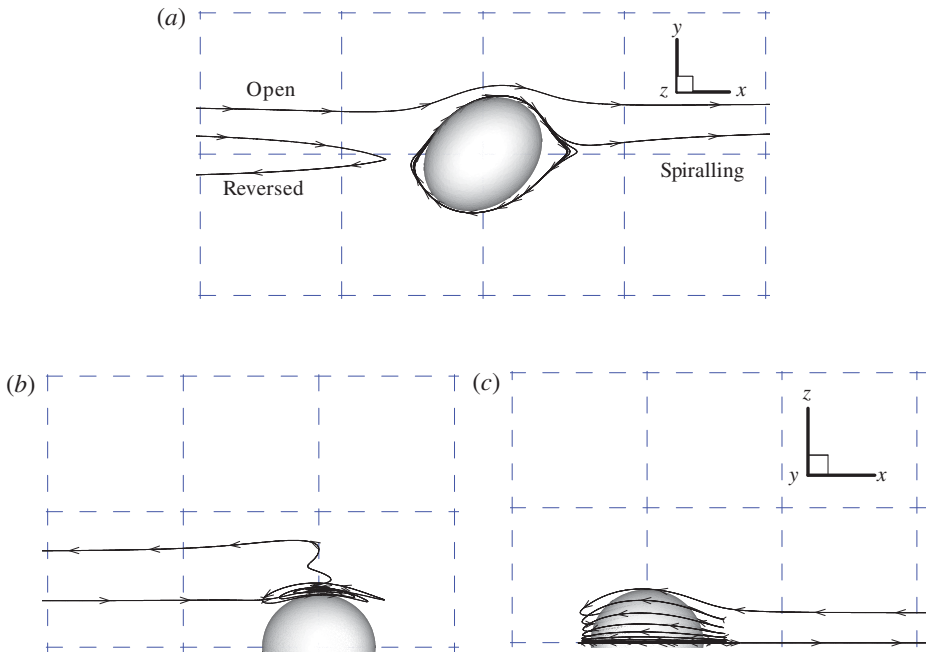

FIGURE 9. (Colour online) (*a*) In-plane open streamline, reversed streamline (through $-1.98a$, 0, 0) and spiralling streamline (through $-1.1a$, 0, 0) around a drop at $Re = 0.50$ and $Ca = 0.10$. Projection of off-plane spiralling streamlines in x–z plane (*b*) through ($-0.05a$, 0, $2a$) and (*c*) through ($-1.15a$, 0, $0.5a$).

at larger Reynolds numbers for larger Ca values. First-order perturbation analysis for small capillary and Reynolds numbers has shown that the effective first and second normal stress differences in a dilute emulsion change sign for critical values of the Ohnesorge number $Oh = \sqrt{Ca/Re} - Oh = 0.32$ and $Oh = 0.43$, respectively, for first and second normal stress differences (Raja *et al.* 2010). As mentioned before, the effective extra stress, including its sign change, in an emulsion is dominated by the contribution due to the interfacial stresses. The interfacial stress differences plotted as a function of Oh (figure 8*c*, *d*) show that they change sign over two small ranges of Ohnesorge numbers – $Oh \sim 0.1 - 0.3$ for $q_{11} - q_{22}$ and $Oh \sim 0.25 - 0.4$ for $q_{22} - q_{33}$. Note that the higher values of Oh are obtained for lower Reynolds numbers. These results are close to the perturbation results. In § 3.2, we discussed the reason behind the Ohnesorge dependence. The inclination angle plotted in figure 7(*a*) indicates that, for small capillary numbers, the critical Re for $\varphi > \pi/4$ indeed varies approximately linearly, consistent with this observation.

3.4. *Streamline patterns around the drop*

In figure 9, we show in-plane and off-plane streamlines around a drop ($\lambda = 1$) at $Re = 0.50$ and $Ca = 0.10$. We see three types of in-plane streamlines – open, reversed and spiralling – around the drop (figure 9*a*), similar to those found for a rigid sphere. However, reversed and spiralling streamlines here becomes further distorted; drop deformation and its inclination result in gradient direction movement of saddle points on both sides distorting the streamlines.

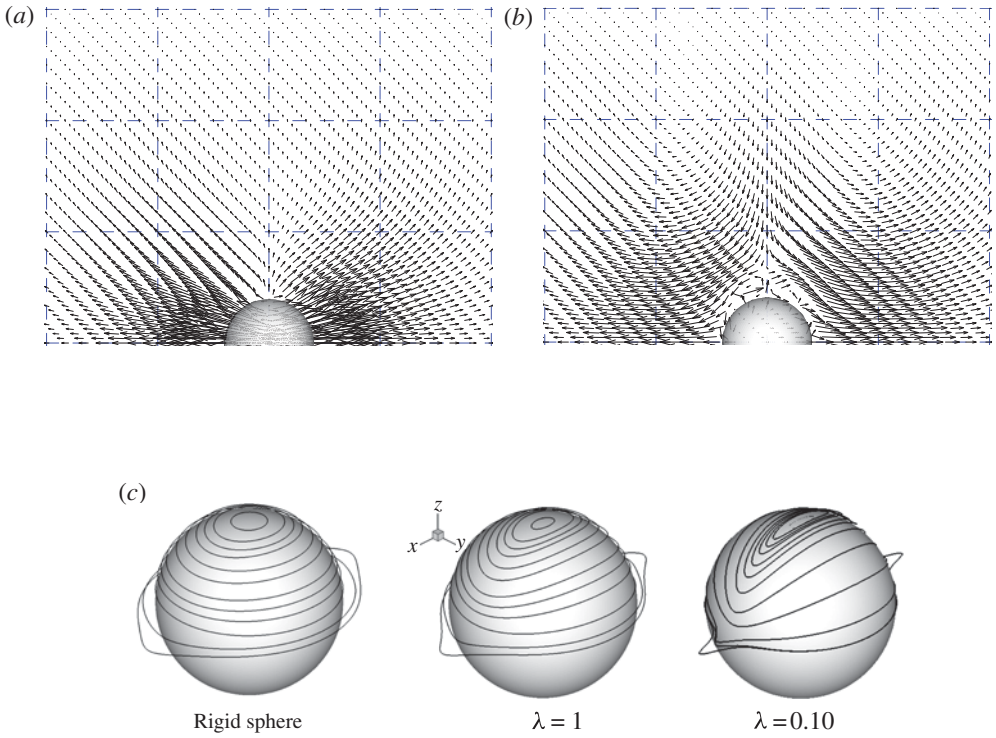

FIGURE 10. (Colour online) Velocity field in the $x = 0$ plane for (a) a 'drop at $Re = 0.50$ and $Ca = 0.10$, and (b) a rigid sphere at $Re = 0.50$. (c) Stokes flow streamlines around a rigid sphere and drops with two viscosity ratios $\lambda = 1.0$ and $\lambda = 0.1$.

In figures 9(b) and 9(c), we plot the projection of an off-plane spiralling streamline in the x–z plane. In figure 9(b), an off-plane streamline moves away from the central plane $z = 0$, rather than coming towards it as is seen for rigid particles (figure 3b). However, streamlines starting near the central plane spiral towards it (figure 9c). The flow field governs streamlines. The spiralling away from or towards the central plane can be understood by the flow field in the $x = 0$ plane, shown in figure 10(a) for a drop, and figure 10(b) for a rigid sphere. For a drop, in contrast to a rigid sphere, velocity near the drop tip in the z direction moves outward (away from the $z = 0$ plane). Note that the imposed shear results in a perturbed flow field with only a very weak z-dependence, which finally determines the direction of movement in the vorticity direction of a particular streamline. Plotted streamlines are based on a $144 \times 144 \times 144$ computational grid. Note that the velocity is computed interpolating from the discrete grid to the front vertices, and is therefore only approximate. We make sure that the streamlines retain their qualitative features upon grid refinement and domain size variation (figure 11 shows 4 different simulations of the same streamline plotted in figure 9b with different domain sizes and grid resolutions).

In § 3.1, we have given the physical arguments for streamlines spiralling towards the central plane, in terms of the inertial effects on the streamline curvature in the x–y plane. However, note also that because of the curvature of the sphere in the x–z plane, a streamline has to curve in the z direction as it flows past the sphere (figure 9b,c). To understand this further, we investigate the first order in Ca flow field

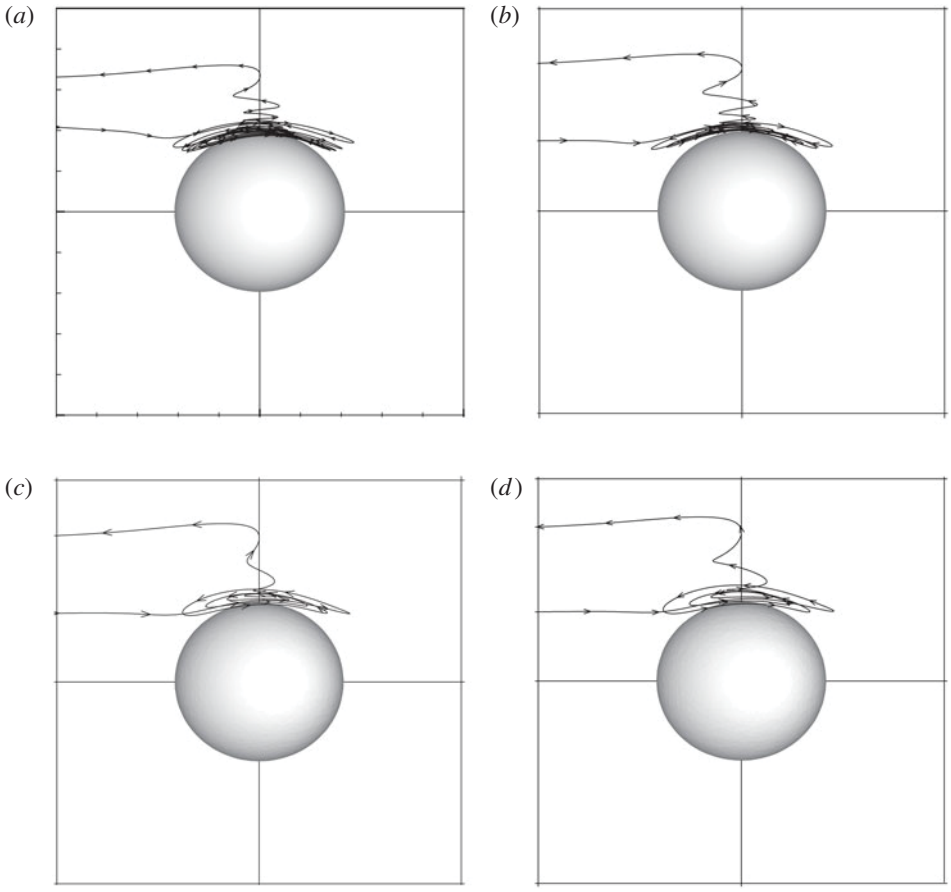

FIGURE 11. Plot showing the same off-plane spiralling streamline around a drop at $Re = 0.50$, $Ca = 0.10$ and $\lambda = 1$ in different grid resolutions (grid points $GP/5a$) and domain sizes: (*a*) $5a \times 5a \times 5a$, $168GP/5a$; (*b*) $10a \times 10a \times 15a$, $72GP/5a$; (*c*) $15a \times 15a \times 15a$, $48GP/5a$; (*d*) $20a \times 20a \times 20a$, $72GP/5a$.

around a drop in shear in a Stokes flow (Leal 2007) ($i = 1, 2, 3$ corresponds to x, y, and z, $r = |\mathbf{x}|$):

$$u_i = \frac{\dot{\gamma}}{2}(\delta_{i1}x_2 + \delta_{i2}x_1)\left(1 - \frac{\lambda}{\lambda+1}\frac{1}{r^5}\right) + \frac{\dot{\gamma}}{2}(\delta_{i1}x_2 - \delta_{i2}x_1) - \frac{\dot{\gamma}}{2}x_1x_2x_i\left(\frac{5\lambda+2}{(\lambda+1)}\frac{1}{r^5} - \frac{5\lambda}{(\lambda+1)}\frac{1}{r^7}\right). \tag{3.6}$$

Here $\lambda \to \infty$ gives the exact Stokes solution around a rigid sphere in shear. In figure 10(*c*), we plot closed streamlines near a rigid sphere and drops with two viscosity ratios. One sees that the curvature away from the x–y plane is minimal for the rigid sphere, and increases with decreasing viscosity ratio. This curvature causes centrifugal force moving a fluid particle away in the z direction with increasing inertia, and thus leading to spiralling away from the central shear plane. Note that this centrifugal force is maximal near the tip of the drop in the vorticity direction. This

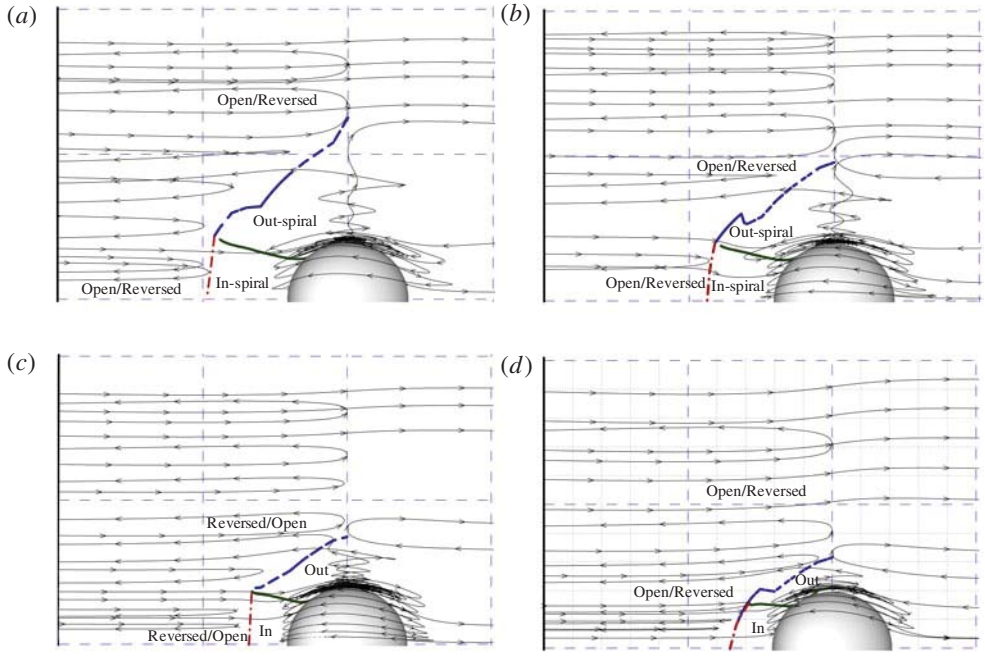

FIGURE 12. (Colour online) Effects of inertia on zones of three different types of off-plane streamlines around a drop at $Ca = 0.10$ and $\lambda = 1$. (*a*) $Re = 0.05$, (*b*) $Re = 0.20$, (*c*) $Re = 0.50$, (*d*) $Re = 1.0$.

leads to the zone near the drop's tip in the z direction, where flow is outward from the $z = 0$ plane.

In figure 12, the streamline pattern around a drop is investigated for increasing Reynolds number. For each Reynolds number, it delineates the zones of (i) streamlines spiralling outward in the vorticity direction, (ii) streamlines spiralling inward near the central plane, and (iii) the region of open and reversed streamlines. Similar to the rigid-sphere case (figure 4), we see that there is a distance z_s in the vorticity direction beyond which there is no spiralling streamline. However, the zone of inward spiralling streamlines seems to be unaffected by increasing inertia. The figures plotted in the x–z plane show a projection of the streamlines. Consistent with the direction of spiralling for the spiralling streamlines, the reversed streamlines at the same z distance show a change in direction: close to the central plane a reversed streamline flows inward towards the central plane, but further away (at larger z value), it goes away from the central plane. We also see that increasing inertia decreases the number of turns in a spiralling streamline, similar to other findings for a rigid sphere (Kulkarni & Morris 2008*a*). The limiting distance z_s is plotted in figure 13 for several capillary numbers as a function of Reynolds number. Similar to the rigid particle case, increasing the Reynolds number shrinks the extent of spiralling streamline (smaller z_s). z_s is less for drops than for rigid spheres. Increasing the capillary number reduces z_s even further.

3.5. *Effect of the viscosity ratio* λ *on the spiralling streamline*

In Stokes flow, an increased viscosity ratio aligns a drop away from the extensional axis towards the flow direction. On the other hand, increased inertia tends to incline it away from the flow direction. Figure 7(*a*) shows that the drop inclination

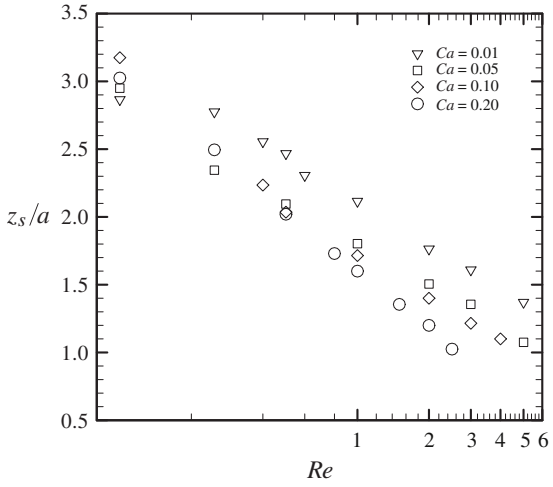

FIGURE 13. Plot showing the variation of z_s, the extent of spiralling streamline, with Re at different Ca.

becomes $\varphi > \pi/4$ with increasing Re, especially for the two lowest capillary numbers ($Ca = 0.01$ and 0.05). We investigate the competing effects of inertia and viscosity ratio increase for the same two cases in figure 14.

The inclination angle predictably decreases with increasing viscosity ratio, with the effect less for the lower-capillary-number case $Ca = 0.01$. The critical value of Re required for $\varphi > \pi/4$ increases with λ. For large enough λ, $\varphi > \pi/4$ does not occur for the Reynolds number range considered here. Note that for rigid particles ($\lambda \to \infty$), spiralling streamlines move towards the central plane, whereas for drops they move away from the central plane near the tip. In figure 15, we consider this effect by plotting off-plane streamlines in the x–z plane. We delineate the three zones: (i) open/reversed streamlines, (ii) streamlines spiralling inward towards the central plane close to it and near the drop surface, and (iii) streamlines spiralling away from the central plane near the drop tip at $Re = 1.0$ and $Ca = 0.10$ for four viscosity ratios. As can be seen, at the highest viscosity ratio of $\lambda = 25$ (as well as all higher-viscosity ratios), the zone of outward spiralling streamlines disappear, and we only see streamlines spiralling towards the central plane as in the case of a rigid sphere. For lower Reynolds numbers, the viscosity ratio above which the streamlines only spiral inward is higher (not shown here for brevity).

4. Summary

We numerically investigate the effects of inertia on the flow field around a drop in shear using the front-tracking finite difference method. Small-inertia perturbation analysis previously showed that inertia destroys closed streamlines around a sheared rigid sphere in Stokes flow. Here, we show that for drops and rigid spheres, it creates reversed as well as spiralling streamlines. We show that the direction of movement of the spiralling streamlines can be either towards the central shear plane or away from it. The movement of the streamlines can be explained by noting the inertial centrifugal force on a fluid particle as it moves around a rigid sphere or a drop. Inertia also causes oscillation in the deformation of the drop before settling in a steady state. The oscillation dynamics is explained with the help of a simple harmonic oscillator model

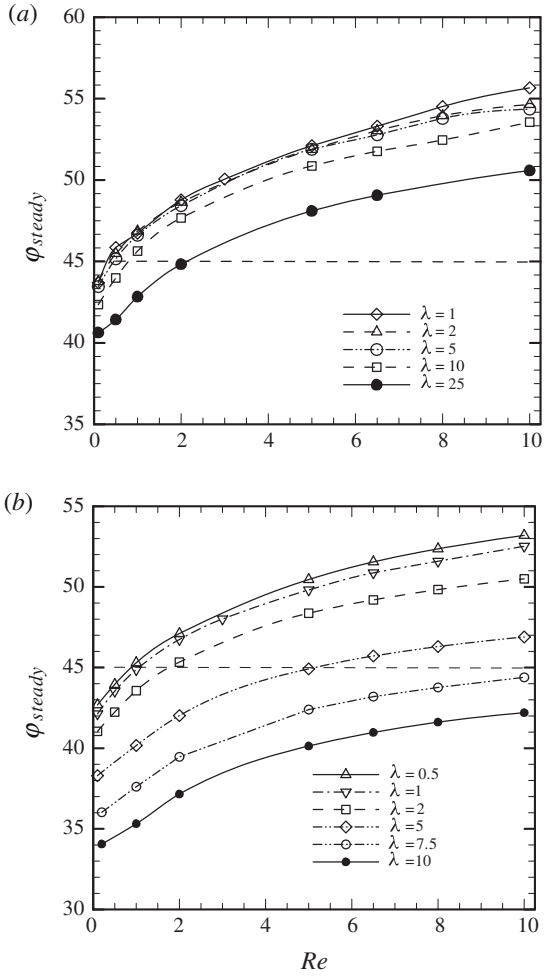

FIGURE 14. Effects of viscosity ratio on the orientation angle with Reynolds number at (*a*) $Ca = 0.01$ and (*b*) $Ca = 0.05$.

that captures the scaling of the oscillation frequency and damping with Reynolds and capillary numbers. Inertia causes the drop to incline more than 45° with the flow direction at low capillary numbers. We investigate dispersed stresses due to the drop, specifically the first and second normal interface tensor differences. The altered inclination causes these components to change sign – first interface tensor difference from positive to negative and second normal interface tensor difference from negative to positive – the effect being greater at low capillary numbers. These effects lead to changes in sign of effective normal stress differences in an emulsion of such drops. At larger capillary numbers, larger deformation at increased inertia leads to drops inclining more to the flow axis. A larger viscosity ratio does the same, and therefore the critical Reynolds number where one sees an inclination angle larger than 45° is greater for higher viscosity ratios. We have delineated the zones of different types of streamlines: (i) open/reversed streamlines, (ii) streamlines spiralling inward towards the central shear plane, (iii) streamlines spiralling outward away from the central plane as a function of viscosity ratio and Reynolds number. Consistent with the rigid-sphere

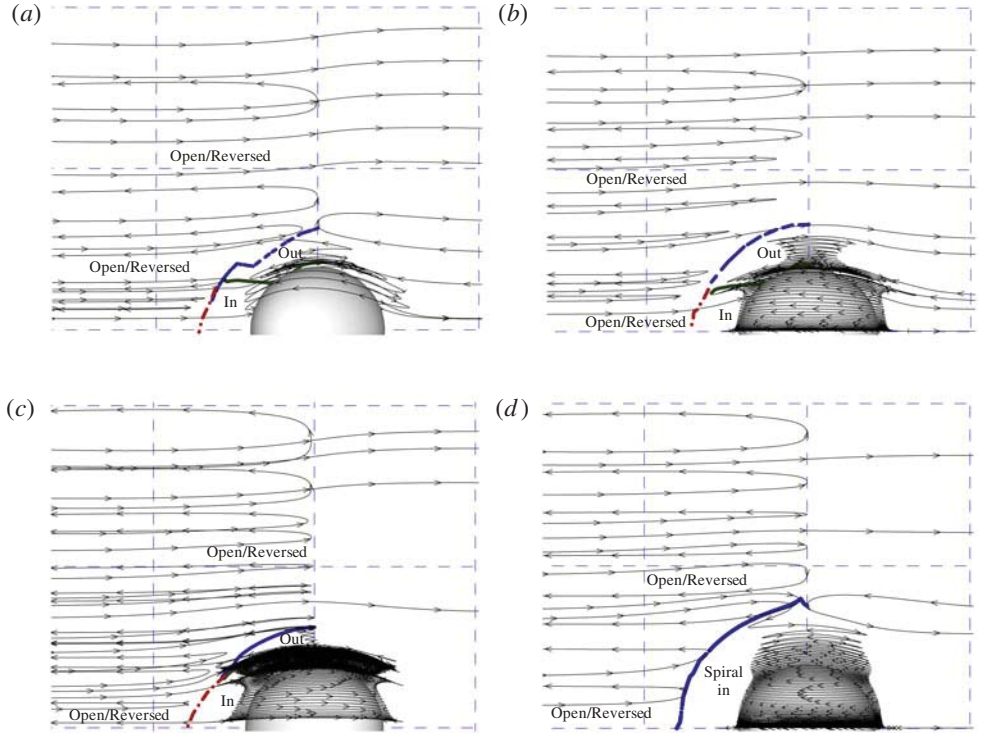

FIGURE 15. (Colour online) Plot showing zones of three different types of off-plane streamlines around a drop at $Re = 1.0$, $Ca = 0.10$ and different viscosity ratios (λ): (a) $\lambda = 1$, (b) $\lambda = 10$, (c) $\lambda = 12.50$, (d) $\lambda = 25$.

case, for sufficiently high viscosity ratio streamlines spiralling away from the central plane disappear.

K.S. acknowledges financial support from NSF grants CBET-0625599 and CBET-0651912. He also acknowledges insightful discussions about streamline spiralling with Professor G. Subramanian of Jawaharlal Nehru Centre for Advanced Scientific Research. The authors also thank the reviewers for helpful comments, particularly one of them for pointing out the possible correlation between Re_{crit} and Ca.

Appendix A

Batchelor (1970) provided a formulation for finding stresses in a suspension of rigid particles. In the appendix, he provided a brief sketch of the contribution due to surface tension. We feel that providing a complete derivation will be helpful to the reader; see also Li & Sarkar (2005*c*), Onuki (1987) and Mellema & Willemse (1983). We follow Batchelor (1970) in defining the average stress in a suspension as a volume average over an averaging volume V, containing drops of volume V_d and enclosing surface A_d, to be

$$\boldsymbol{\sigma}^{ave} = \frac{1}{V}\int_V (\boldsymbol{\sigma} - \rho \boldsymbol{u}'\boldsymbol{u}')\,\mathrm{d}V$$
$$= \frac{1}{V}\left(\left(\int_{V-\sum V_d} + \sum \int_{V_d^+}\right)\boldsymbol{\sigma}\,\mathrm{d}V\right) + \boldsymbol{\sigma}^{ptb}, \quad \boldsymbol{\sigma}^{ptb} = -\frac{1}{V}\int_V \rho \boldsymbol{u}'\boldsymbol{u}'\,\mathrm{d}V, \quad \text{(A 1)}$$

where $\boldsymbol{\sigma}^{ptb}$ is the perturbation stress. V_d^+ denotes the volume of the drop that includes the drop interface, i.e. this volume includes the interfacial stress. To separate the interfacial contribution, we write it as

$$\int_{V_d^+} \boldsymbol{\sigma}\,\mathrm{d}V = \int_{V_d} \boldsymbol{\sigma}\,\mathrm{d}V + \int_{V_d^\varepsilon} \boldsymbol{\sigma}\,\mathrm{d}V, \tag{A 2}$$

where V_d^ε is an infinitesimal annular volume of radial extent ε enclosed by two concentric surfaces A_d^+ and A_d^- that includes the drop interface A_d. We use the identity

$$\boldsymbol{\nabla}\cdot(\boldsymbol{\sigma}\boldsymbol{x}) = (\boldsymbol{\nabla}\cdot\boldsymbol{\sigma})\boldsymbol{x} + \boldsymbol{\sigma} \tag{A 3}$$

and momentum equation to find the contribution due to the interfacial tension:

$$\begin{aligned}
\int_{V_d^\varepsilon} \boldsymbol{\sigma}\,\mathrm{d}V &= \lim_{\varepsilon\to 0}\left[\int_{V_d^\varepsilon} \boldsymbol{\nabla}\cdot(\boldsymbol{\sigma}\boldsymbol{x})\,\mathrm{d}V - \int_{V_d^\varepsilon} \rho\frac{\mathrm{D}\boldsymbol{u}}{\mathrm{D}t}\boldsymbol{x}\,\mathrm{d}V\right]\\
&= \int_{\partial V_d^\varepsilon} (\boldsymbol{\sigma}\cdot\boldsymbol{n})\boldsymbol{x}\,\mathrm{d}A\\
&= \int_{A_d} (\boldsymbol{\sigma}_m\cdot\boldsymbol{n} - \boldsymbol{\sigma}_d\cdot\boldsymbol{n})\boldsymbol{x}\,\mathrm{d}A\\
&= \int_{A_d} \Gamma(\boldsymbol{\nabla}\cdot\boldsymbol{n})\boldsymbol{n}\boldsymbol{x}\,\mathrm{d}A\\
&= \Gamma\int_{A_d} (\boldsymbol{I}-\boldsymbol{n}\boldsymbol{n})\,\mathrm{d}A.
\end{aligned} \tag{A 4}$$

Here the last step is due to an identity proved by Rosenkilde (1967) (equation (14) in that reference). Therefore the interfacial contribution $\boldsymbol{\sigma}^{int}$ to the excess stress is

$$\boldsymbol{\sigma}^{int} = \frac{\Gamma}{V}\sum \boldsymbol{q}, \quad \text{where } \boldsymbol{q} = \int_{A_d} (\boldsymbol{I}-\boldsymbol{n}\boldsymbol{n})\,\mathrm{d}A. \tag{A 5}$$

Therefore, the average stress is

$$\begin{aligned}
\boldsymbol{\sigma}^{ave} &= \frac{1}{V}\left(\int_{V-\sum V_d} + \sum\int_{V_d} \boldsymbol{\sigma}\,\mathrm{d}V\right) + \boldsymbol{\sigma}^{int} + \boldsymbol{\sigma}^{ptb}\\
&= -P^{avg}\boldsymbol{I} + \frac{1}{V}\left(\int_{V-\sum V_d} \mu_m(\boldsymbol{\nabla}\boldsymbol{u} + \boldsymbol{\nabla}\boldsymbol{u}^{\mathrm{T}})\mathrm{d}V\right.\\
&\quad \left. + \sum\int_{V_d} \mu_d(\boldsymbol{\nabla}\boldsymbol{u} + \boldsymbol{\nabla}\boldsymbol{u}^{\mathrm{T}})\,\mathrm{d}V\right) + \boldsymbol{\sigma}^{int} + \boldsymbol{\sigma}^{ptb}\\
&= -P^{avg}\boldsymbol{I} + \frac{1}{V}\left(\int_{V} \mu_m(\boldsymbol{\nabla}\boldsymbol{u} + \boldsymbol{\nabla}\boldsymbol{u}^{\mathrm{T}})\,\mathrm{d}V\right.\\
&\quad \left. + \sum\int_{V_d} (\mu_d-\mu_m)(\boldsymbol{\nabla}\boldsymbol{u} + \boldsymbol{\nabla}\boldsymbol{u}^{\mathrm{T}})\,\mathrm{d}V\right) + \boldsymbol{\sigma}^{int} + \boldsymbol{\sigma}^{ptb}\\
&= -P^{avg}\boldsymbol{I} + \mu_m(\boldsymbol{\nabla}\boldsymbol{u}^{avg} + \boldsymbol{\nabla}\boldsymbol{u}^{avg\,\mathrm{T}})\\
&\quad + \frac{1}{V}\sum(\mu_d-\mu_m)\int_{A_d} (\boldsymbol{n}\boldsymbol{u} + \boldsymbol{u}\boldsymbol{n})\,\mathrm{d}A + \boldsymbol{\sigma}^{int} + \boldsymbol{\sigma}^{ptb}\\
&= -P^{avg}\boldsymbol{I} + \mu_m(\boldsymbol{\nabla}\boldsymbol{u}^{avg} + \boldsymbol{\nabla}\boldsymbol{u}^{avg\,\mathrm{T}}) + \boldsymbol{\sigma}^{vis} + \boldsymbol{\sigma}^{int} + \boldsymbol{\sigma}^{ptb},
\end{aligned} \tag{A 6}$$

where

$$\boldsymbol{\sigma}^{vis} = \frac{1}{V}\sum \mu_m(\lambda - 1)\int_{A_d} \boldsymbol{nu} + \boldsymbol{un}\,\mathrm{d}A. \tag{A 7}$$

We note that the interface tensor $\boldsymbol{q}_d$, which is a purely geometric quantity, is important for determining the overall rheology of the emulsion.

Appendix B

The interface tensor also appears in the far-field perturbation velocity field due to a drop suspended in a Stokes flow. We write the exterior velocity field as a combination of the imposed shear field $\boldsymbol{u}^\infty$ and a perturbation,

$$\boldsymbol{u} = \boldsymbol{u}^\infty + \boldsymbol{u}^d, \tag{B 1}$$

and inside the drop as $\tilde{\boldsymbol{u}}$. Using the standard free space Green's function (vanishing at infinity) of the Stokes flow (Pozrikidis 1992), one can write the perturbation velocity field outside a drop as an integral over the drop surface

$$\left.\begin{aligned} u_j^d(\boldsymbol{x}) &= -\frac{1}{8\pi\mu_m}\int_{A_d} f_i^d(\boldsymbol{y})G_{ij}(\boldsymbol{x},\boldsymbol{y})\,\mathrm{d}A(\boldsymbol{y}) \\ &\quad + \frac{1}{8\pi}\int_{A_d} u_i^d(\boldsymbol{y})T_{ijk}(\boldsymbol{x},\boldsymbol{y})n_k(\boldsymbol{y})\,\mathrm{d}A(\boldsymbol{y}), \\ G_{ij}(\boldsymbol{x},\boldsymbol{y}) &= \frac{\delta_{ij}}{|\boldsymbol{x}-\boldsymbol{y}|} + \frac{(x_i - y_i)(x_j - y_j)}{|\boldsymbol{x}-\boldsymbol{y}|^3}, \\ T_{ijk}(\boldsymbol{x},\boldsymbol{y}) &= -6\frac{(x_i - y_i)(x_j - y_j)(x_k - y_k)}{|\boldsymbol{x}-\boldsymbol{y}|^5}, \end{aligned}\right\} \tag{B 2}$$

where $f_i^d = \sigma_{ij}^d n_j$ is the traction vector resulting from the viscous stress $\boldsymbol{\sigma}$ appropriate for the Newtonian flow, and $\boldsymbol{n}$ is the outward normal to V_d. Writing a similar expression inside V_d for the imposed shear field $\boldsymbol{u}^\infty$ and noting that $\boldsymbol{x}$ is outside V_d, we obtain

$$0 = -\frac{1}{8\pi\mu_m}\int_{A_d} f_i^\infty(\boldsymbol{y})G_{ij}(\boldsymbol{x},\boldsymbol{y})\,\mathrm{d}A(\boldsymbol{y}) + \frac{1}{8\pi}\int_{A_d} u_i^\infty(\boldsymbol{y})T_{ijk}(\boldsymbol{x},\boldsymbol{y})n_k(\boldsymbol{y})\,\mathrm{d}A(\boldsymbol{y}). \tag{B 3}$$

One can add (B 2) and (B 3) to find the complete velocity field $\boldsymbol{u}$ (note that $\boldsymbol{f} = \boldsymbol{f}^\infty + \boldsymbol{f}^d$) outside the drop:

$$\begin{aligned} u_j(\boldsymbol{x}) = u_j^\infty(\boldsymbol{x}) &- \frac{1}{8\pi\mu_m}\int_{A_d} f_i(\boldsymbol{y})G_{ij}(\boldsymbol{x},\boldsymbol{y})\,\mathrm{d}A(\boldsymbol{y}) \\ &+ \frac{1}{8\pi}\int_{A_d} u_i(\boldsymbol{y})T_{ijk}(\boldsymbol{x},\boldsymbol{y})n_k(\boldsymbol{y})\,\mathrm{d}A(\boldsymbol{y}). \end{aligned} \tag{B 4}$$

For the interior velocity field $\tilde{\boldsymbol{u}}$ we also write (noting once again that $\boldsymbol{x}$ is outside V_d)

$$0 = \frac{1}{8\pi\mu_d}\int_{A_d} \tilde{f}_i(\boldsymbol{y})G_{ij}(\boldsymbol{x},\boldsymbol{y})\,\mathrm{d}A(\boldsymbol{y}) - \frac{1}{8\pi}\int_{A_d} \tilde{u}_i(\boldsymbol{y})T_{ijk}(\boldsymbol{x},\boldsymbol{y})n_k(\boldsymbol{y})\,\mathrm{d}A(\boldsymbol{y}). \tag{B 5}$$

Adding the expression for the exterior velocity field to (B 5) multiplied by λ, we obtain

$$u_j(\boldsymbol{x}) = u_j^\infty(\boldsymbol{x}) - \frac{1}{8\pi\mu_m}\int_{A_d} \Delta f_i(\boldsymbol{y})G_{ij}(\boldsymbol{x},\boldsymbol{y})\,\mathrm{d}A(\boldsymbol{y})$$

$$+\frac{(1-\lambda)}{8\pi}\int_{A_d} u_i(\boldsymbol{y})T_{ijk}(\boldsymbol{x},\boldsymbol{y})n_k(\boldsymbol{y})\,\mathrm{d}A(\boldsymbol{y}), \tag{B 6}$$

where

$$\Delta\boldsymbol{f} = (\boldsymbol{f} - \tilde{\boldsymbol{f}}) = \Gamma(\boldsymbol{\nabla}\cdot\boldsymbol{n})\boldsymbol{n}, \tag{B 7}$$

and continuity on velocity has been used. Now for an expression appropriate for the far field, we expand $G_{ij}(\boldsymbol{x},\boldsymbol{y})$ in a Taylor series around the centre of the drop $\boldsymbol{y}_c$,

$$G_{ij}(\boldsymbol{x},\boldsymbol{y}) = G_{ij}(\boldsymbol{x},\boldsymbol{y}_c) + \frac{\partial G_{ij}(\boldsymbol{x},\boldsymbol{y}_c)}{\partial y_{ck}}(y_k - y_{ck}) + O\Big(\frac{a}{L}\Big)^3, \tag{B 8a}$$

$$T_{ijk}(\boldsymbol{x},\boldsymbol{y}) = T_{ijk}(\boldsymbol{x},\boldsymbol{y}_c) + O\Big(\frac{a}{L}\Big)^3, \tag{B 8b}$$

and obtain

$$u_j(\boldsymbol{x}) = u_j^{\infty}(\boldsymbol{x}) - \frac{1}{8\pi\mu_m}G_{ij}(\boldsymbol{x},\boldsymbol{y}_c)\int_{A_d}\Delta f_i(\boldsymbol{y})\,\mathrm{d}A(\boldsymbol{y}) - \frac{1}{8\pi\mu_m}\frac{\partial G_{ij}(\boldsymbol{x},\boldsymbol{y}_c)}{\partial y_{ck}} \times \int_{A_d}[\Delta f_i(\boldsymbol{y})(y_k - y_{ck}) - \mu_m(1-\lambda)(u_i n_k + u_k n_i)(\boldsymbol{y})]\,\mathrm{d}A(\boldsymbol{y}), \tag{B 9}$$

noting that $\int_{A_d} u_k(\boldsymbol{y})n_k(\boldsymbol{y})\,\mathrm{d}A(\boldsymbol{y}) = 0$. For a force-free drop, $\int_{A_d}\Delta f_j(\boldsymbol{y})\,\mathrm{d}A(\boldsymbol{y}) = 0$. We obtain

$$u_j(\boldsymbol{x}) = u_j^{\infty}(\boldsymbol{x}) - \frac{1}{8\pi\mu_m}\frac{\partial G_{ij}(\boldsymbol{x},\boldsymbol{y}_c)}{\partial y_{ck}} \times \left\{\Gamma\int_{A_d}(\boldsymbol{I}-\boldsymbol{nn})\,\mathrm{d}A - \mu_m(1-\lambda)\int_{A_d}(u_i n_k + u_k n_i)\,\mathrm{d}A(\boldsymbol{y})\right\}, \tag{B 10}$$

where once again the last relation in (A 4), due to Rosenkilde (1967), is used. Note that the expressions in brackets also appear in (A 5) and (A 7) in Appendix A.

REFERENCES

ACRIVOS, A. 1971 Heat transfer at high Péclet number from a small sphere freely rotating in a simple shear field. *J. Fluid Mech.* **46**, 233–240.

AGGARWAL, N. & SARKAR, K. 2007 Deformation and breakup of a viscoelastic drop in a Newtonian matrix under steady shear. *J. Fluid Mech.* **584**, 1–21.

AGGARWAL, N. & SARKAR, K. 2008*a* Effects of matrix viscoelasticity on viscous and viscoelastic drop deformation in a shear flow. *J. Fluid Mech.* **601**, 63–84.

AGGARWAL, N. & SARKAR, K. 2008*b* Rheology of an emulsion of viscoelastic drops in steady shear. *J. Non-Newtonian Fluid Mech.* **150**, 19–31.

ALMUSALLAM, A. S., LARSON, R. G. & SOLOMON, M. J. 2004 Comprehensive constitutive model for immiscible blends of Newtonian polymers. *J. Rheol.* **48**, 319–348.

BATCHELOR, G. K. 1970 Stress system in a suspension of force-free particles. *J. Fluid Mech.* **41**, 545–570.

CHAFFEY, C. E. & BRENNER, H. 1967 A second order theory for shear deformation of drops. *J. Colloid Interface Sci.* **24**, 258–269.

CHOI, S. J. & SCHOWALTER, W. R. 1975 Rheological properties of non-dilute suspensions of deformable particles. *Phys. Fluids* **18**, 420–427.

GUIDO, S. & SIMEONE, M. 1998 Binary collision of drops in simple shear flow by computer-assisted video optical microscopy. *J. Fluid Mech.* **357**, 1–20.

GUIDO, S. & VILLONE, M. 1998 Three-dimensional shape of a drop under simple shear flow. *J. Rheol.* **42**, 395–415.

KOSSACK, C. A. & ACRIVOS, A. 1974 Steady simple shear flow past a circular cylinder at moderate Reynolds numbers: a numerical solution. *J. Fluid Mech.* **66**, 353–376.

KULKARNI, P. M. & MORRIS, J. F. 2008*a* Pair-sphere trajectories in finite-Reynolds-number shear flow. *J. Fluid Mech.* **596**, 413–435.

KULKARNI, P. M. & MORRIS, J. F. 2008*b* Suspension properties at finite Reynolds number from simulated shear flow. *Phys. Fluids* **20**, 040602.

LEAL, L. G. 1980 Particle motions in a viscous fluid. *Annu. Rev. Fluid Mech.* **12**, 435–476.

LEAL, L. G. 2007 *Advanced Transport Phenomena: Fluid Mechanics and Convective Transport*. Cambridge University Press.

LI, X. & SARKAR, K. 2005*a* Negative normal stress elasticity of emulsion of viscous drops at finite inertia. *Phys. Rev. Lett.* **95**, 256001.

LI, X. Y. & SARKAR, K. 2005*b* Drop dynamics in an oscillating extensional flow at finite Reynolds numbers. *Phys. Fluids* **17**, 027103.

LI, X. Y. & SARKAR, K. 2005*c* Effects of inertia on the rheology of a dilute emulsion of drops in shear. *J. Rheol.* **49**, 1377–1394.

LI, X. Y. & SARKAR, K. 2005*d* Numerical investigation of the rheology of a dilute emulsion of drops in an oscillating extensional flow. *J. Non-Newtonian Fluid Mech.* **128**, 71–82.

LI, X. Y. & SARKAR, K. 2006 Drop deformation and breakup in a vortex at finite inertia. *J. Fluid Mech.* **564**, 1–23.

LIN, C. J., PERRY, J. H. & SCHOWALTER, W. R. 1970 Simple shear flow round a rigid sphere: inertial effects and suspension rheology. *J. Fluid Mech.* **44**, 1–17.

MELLEMA, J. & WILLEMSE, M. W. M. 1983 Effective viscosity of dispersions approached by a statistical continuum method. *Physica* A **122**, 286–312.

MIKULENCAK, D. R. & MORRIS, J. F. 2004 Stationary shear flow around fixed and free bodies at finite Reynolds number. *J. Fluid Mech.* **520**, 215–242.

MUKHERJEE, S. & SARKAR, K. 2009 Effects of viscosity ratio on deformation of a viscoelastic drop in a Newtonian matrix under steady shear. *J. Non-Newtonian Fluid Mech.* **160**, 104–112.

MUKHERJEE, S. & SARKAR, K. 2010 Effects of viscoelasticity on the retraction of a sheared drop. *J. Non-Newtonian Fluid Mech.* **165**, 340–349.

MUKHERJEE, S. & SARKAR, K. 2011 Viscoelastic drop falling through a viscous medium. *Phys. Fluids* **23**, 013101.

OLAPADE, P. O., SINGH, R. K. & SARKAR, K. 2009 Pair-wise interactions between deformable drops in free shear at finite inertia. *Phys. Fluids* **21**, 063302.

ONUKI, A. 1987 Viscosity enhancement by domains in phase-separating fluids near the critical point: proposal of critical rheology. *Phys. Rev.* A **35**, 5149–5155.

POE, G. G. & ACRIVOS, A. 1975 Closed-streamline flows past rotating single cylinders and spheres: inertia effects. *J. Fluid Mech.* **72**, 605–623.

POZRIKIDIS, C. 1992 *Boundary Integral and Singularity Methods for Linearized Viscous Flow*. Cambridge University Press.

RAJA, R. V., SUBRAMANIAN, G. & KOCH, D. L. 2010 Inertial effects on the rheology of a dilute emulsion. *J. Fluid Mech.* **646**, 255–296.

RALLISON, J. M. 1980 Note on the time-dependent deformation of a viscous drop which is almost spherical. *J. Fluid Mech.* **98**, 625–633.

RENARDY, Y. 2008 Effect of startup conditions on drop breakup under shear with inertia. *Intl J. Multiphase Flow* **34**, 1185–1189.

RENARDY, Y. Y. & CRISTINI, V. 2001*a* Effect of inertia on drop breakup under shear. *Phys. Fluids* **13**, 7–13.

RENARDY, Y. Y. & CRISTINI, V. 2001*b* Scalings for fragments produced from drop breakup in shear flow with inertia. *Phys. Fluids* **13**, 2161–2164.

ROBERTSON, C. R. & ACRIVOS, A. 1970*a* Low Reynolds number shear flow past a rotating circular cylinder. Part 1. Momentum transfer. *J. Fluid Mech.* **40**, 685–704.

ROBERTSON, C. R. & ACRIVOS, A. 1970*b* Low Reynolds number shear flow past a rotating circular cylinder. Part 2. Heat transfer. *J. Fluid Mech.* **40**, 705–718.

ROSENKILDE, C. E. 1967 Surface-energy tensors. *J. Math. Phys.* **8**, 84–88.

SARKAR, K. & SCHOWALTER, W. R. 2000 Deformation of a two-dimensional viscoelastic drop at non-zero Reynolds number in time-periodic extensional flows. *J. Non-Newtonian Fluid Mech.* **95**, 315–342.

SARKAR, K. & SCHOWALTER, W. R. 2001*a* Deformation of a two-dimensional drop at non-zero Reynolds number in time-periodic extensional flows: numerical simulation. *J. Fluid Mech.* **436**, 177–206.

SARKAR, K. & SCHOWALTER, W. R. 2001*b* Deformation of a two-dimensional viscous drop in time-periodic extensional flows: analytical treatment. *J. Fluid Mech.* **436**, 207–230.

SIBILLO, V., PASQUARIELLO, G., SIMEONE, M., CRISTINI, V. & GUIDO, S. 2006 Drop deformation in microconfined shear flow. *Phys. Rev. Lett.* **97**, 054502.

SINGH, R. K. & SARKAR, K. 2009 Effects of viscosity ratio and three dimensional positioning on hydrodynamic interactions between two viscous drops in a shear flow at finite inertia. *Phys. Fluids* **21**, 103303.

STONE, H. A. 1994 Dynamics of drop deformation and breakup in viscous fluids. *Annu. Rev. Fluid Mech.* **26**, 65–102.

SUBRAMANIAN, G. & BRADY, J. F. 2006 Trajectory analysis for non-Brownian inertial suspensions in simple shear flow. *J. Fluid Mech.* **559**, 151–203.

SUBRAMANIAN, G. & KOCH, D. L. 2006*a* Centrifugal forces alter streamline topology and greatly enhance the rate of heat and mass transfer from neutrally buoyant particles to a shear flow. *Phys. Rev. Lett.* **96**, 134503.

SUBRAMANIAN, G. & KOCH, D. L. 2006*b* Inertial effects on the transfer of heat or mass from neutrally buoyant spheres in a steady linear velocity field. *Phys. Fluids* **18**, 073302.

TANAKA, H. & ARAKI, T. 2000 Simulation method of colloidal suspensions with hydrodynamic interactions: fluid particle dynamics. *Phys. Rev. Lett.* **85**, 1338–1341.

TAYLOR, G. I. 1934 The formation of emulsions in definable fields of flow. *Proc. R. Soc. Lond.*A *Math. Phys. Sci.* **146**, 0501–0523.

TRYGGVASON, G., BUNNER, B., ESMAEELI, A., JURIC, D., AL-RAWAHI, N., TAUBER, W., HAN, J., NAS, S. & JAN, Y. J. 2001 A front-tracking method for the computations of multiphase flow. *J. Comput. Phys.* **169**, 708–759.

UNVERDI, S. O. & TRYGGVASON, G. 1988 A front-tracking method for viscous, incompressible multi-fluid flows. *J. Comput. Phys.* **100**, 25–37.